A novel quasi-one-dimensional model for performance estimation of a Vaporizing Liquid Microthruster

M.G. De Giorgi[a,*], D. Fontanarosa[a]

[a] *University of Salento, Dep. of Engineering for Innovation, Via per Monteroni, 73100-Lecce, Italy*

Abstract

The present work aims to propose a novel quasi-one-dimensional model for the performance estimation of a Vaporizing Liquid Microthruster (VLM). The analytical model was applied to the analysis of a MEMS-based VLM composed of a rectangular inlet chamber, a set of parallel microchannels as heating chamber, and a planar convergent-divergent micronozzle. It combines a steady-state boiling model for the analysis of the heater with a real nozzle flow model for the evaluation of actual thrust force and specific impulse, based on iterative procedure aiming at the convergence of the actual mass flow rate and the heat flux. For the purpose, a set of semi-empirical formulas found among both theoretical and experimental scientific works have been introduced for the estimation of the critical heat flux condition and the local heat transfer coefficient. In addition, the real nozzle flow model predicts the performance and the viscous losses due to the boundary layer growth inside the micronozzle. The last ones are estimated by introducing analytical expressions for the discharge coefficient and the I_{sp}-efficiency into the isentropic nozzle flow theory. The resulting performance predictions of the 1D model referred to the on-design operating conditions. They well agreed with the experimental data, with a maximum estimated error of 7.3% on the thrust and the specific impulse. Furthermore, the analytical model

*Corresponding author. Address: University of Salento, Dep. of Engineering for Innovation, Research Center for Energy and Environment (UNISALENTO-DII-CREA), Via per Monteroni, LECCE I-73100, Italy. Tel: +39 0832297759.

Email addresses: mariagrazia.degiorgi@unisalento.it (M.G. De Giorgi), donato.fontanarosa@unisalento.it (D. Fontanarosa)

of the micronozzle predicted a reduction of the mass flow rate up to about 8%, as well as thrust losses up to 15% due to the contraction of the cross sectional area.

In addition, 2D and 3D computational fluid dynamics (CFD) simulations were performed in order to enforce the analysis of the viscous effects. Predictions of 2D computations overestimated the performances of the microthruster with respect to experiments, up to about 19% of the thrust and 20% of the specific impulse. On the other hand, the 3D predicted thrust approached to the experimental one with an error of about 9.2% below. In addition, a severe reduction of jet thrust in favor of the pressure thrust was observed at the nozzle exit. Furthermore, 3D computations pointed out the influence of the micronozzle depth on the boundary layer growth and the viscous losses. In particular, they revealed the establishment of the nozzle blockage and the thermal chocking of the supersonic flow owing to the subsequent viscous heating.

Keywords: micro-propulsion, Vaporizing Liquid Microthruster, performance analysis, planar micronozzles, analytical modeling, Computational Fluid Dynamics

---

Nomenclature

Symbols

A_{cs}	cross section are, m^2
Bo	Boiling number, $Bo = \frac{\dot{q}}{h_L G}$
C_d	discharge coefficient$C_d = \frac{\dot{m}_{act}}{\dot{m}_{IRT}}$, $-$
c_p	specific heat at constant pressure, $J/kg/K$
c_v	specific heat at constant volume, $J/kg/K$
D_h	hydraulic diameter $D_h = \frac{4A_{cs}}{P_{cs}}$, m
E	specific total energy, $[kJ/kg]$
Eo	Eotvos number, $Eo = \frac{g_0(\rho_l - \rho_v)\ D_h^2}{\sigma}$

	Fr	Froude number, $Fr = \frac{G^2}{\rho_l g_0 D_h}$
	G	mass flow rate per unit cross section area, $kg/s/m^2$
	g_0	gravitational acceleration, m/s^2
	H	total enthalpy, J
	h	specific enthalpy, J/kg
	h_b	heat transfer coefficient, $W/m^2/K$
	h_L	latent heat of vaporization, J/kg
	I_{sp}	specific impulse, $[s]$
	ΔJ	variation of jet momentum, N
	La	Laplace number, $La = \frac{\rho_l \sigma D_h}{\mu}$
	M	Mach number, $-$
	$\bar{M}_{gas}$	propellant molar weight, $[kg/mol]$
	$\dot{m}$	mass flow rate, kg/s
	Nu	Nusselt number, $Nu = \frac{h_b \, D_h}{\kappa_{cond}}$
	p	static pressure, Pa
	P_{cs}	cross section perimeter, m
	Pr	Prandtl number, $Pr = \frac{c_p \mu}{\kappa_{cond}}$
	$\dot{Q}$	heat power, W
	$\dot{q}$	heat flux, W/m^2
	r_c	radius of curvature of the nozzle throat, m
	R_{gas}	specific gas constant $R_u/\bar{M}_{gas}$, $[J/mol/K]$
	R_u	universal gas constant, $8.314\,\mathrm{J\,mol^{-1}\,K^{-1}}$
	Re	Reynolds number, $Re = \frac{G D_h}{\mu}$
	S	shape factor, $-$
	s	spatial coordinate, m
	T	temperature, K

t	temporal coordinate, s
$\mathbf{u}$	flow velocity vector, m/s
W	width dimension, m
We	Weber number, $We = \frac{G^2 D_h}{\sigma \rho_l}$
x, x_{vap}	mass vapor quality, $-$
X_μ	liquid-to-vapor viscosity ratio, $X_\mu = \frac{\mu_l}{\mu_v}$
X_ρ	liquid-to-vapor density ratio, $X_\rho = \frac{\rho_l}{\rho_v}$
x_{TD}	thermodynamic vapor quality of the water-steam mixture, $\frac{h - h_{l,sat}}{h_L}$
Z_{ch}	channel height, m

Greek Symbols

δ^*	displacement thickness, m
η_u	I_{sp}-efficiency, $\eta_u = \frac{u_{exit,act}}{u_{exit,IRT}}$, $-$
γ	specific heat ratio, $-$
Γ_{VDK}	Vanderkerchoff parameter $\Gamma_{VDK} = \sqrt{\gamma \left(\frac{2}{\gamma - 1}\right)^{\frac{\gamma+1}{\gamma-1}}}$, $-$
κ_{cond}	thermal conductivity, $W/m/K$
μ	dynamic viscosity, $Pa \cdot s$
ρ	fluid density, kg/m^3
σ	surface tension, N/m
τ	viscous stress tensor, $[N/m^2]$
θ	momentum thickness, m
ξ_n	nozzle quality, $-$

Subscripts

$*$	referred to the nozzle throat section
0	referred to stagnation properties
$\bar{(\cdot)}$	referred to the incompressible condition

act	referred to the actual condition
CFD	referred to numerical simulations
$crit$	referred to the critical heat flux condition
d/o	referred to the dry-out condition
DB	referred to the Dittus-Boelter relation
$exit$	referred to the nozzle exit section
$incip$	referred to the incipience of the dry-out condition
$inlet$	referred to the upstream condition
IRT	referred to the Ideal Rocket Theory
j	referred to jet thrust
l	referred to the liquid phase
m	referred to the mixture
num	referred to numerical predictions
$outlet$	referred to the downstream condition
p	referred to pressure thrust
sat	referred to the saturation condition
v	referred to the vapor phase
w	referred to the inner walls

Abbreviations

CFD	Computational Fluid Dynamics
CHF	Critical Heat Flux
DSMC	Direct Simulation Monte Carlo
HTC	Heat Transfer Coefficient
HTCC	High Temperature Co-fired Ceramics
IRT	Ideal Rocket Theory
LTCC	Low Temperature Co-fired Ceramics

MEMS	Micro Electro-Mechanical System
NS	Navier-Stokes
VLM	Vaporizing Liquid Microthruster

1. Introduction

In the last decades, small satellites (total mass less than 20 kg) have found application in academic, industrial and space science programs, thanks to the reduction of the total expenditure of space missions allowed by the advancements in microfabrication technologies. The execution of missions such as orbit transfer or formation flying, requires small thrust forces from few micronewtowns up to some millinewtons, with stringent constraints of mass, volume and power consumption. Consequently, the micro-propulsion system represents a key technology [1]. Several types of Micro-Electric-Mechanical Systems (MEMS) based micro-propulsion system have been proposed, such as cold and hot gas microthrusters (e.g. [2] and [3]), micro-resistojets [4], liquid and solid mono-propellant micro-thrusters ([5], [6] and [7]), plasma micro-thrusters ([8] and [9]), electrospray micro-thrusters [10], just to name a few. A detailed review of micropropulsion systems applied to small satellites can be found in Silva et al. [11]. In the field of the micro-propulsion, micro-resistojets represent an interesting choice since such electro-thermal micro-thrusters are currently able to provide thrust levels in the range $0.1 \div 10\,\mathrm{mN}$ as required for the attitude control and the pointing systems of miniaturized spacecrafts [12], while meeting all mass, volume and power constraints [13]. The propellant can be stored in liquid or solid phase, thus vaporization or sublimation is required prior to the heating of the gas. Devices that use liquid propellants are called Vaporizing Liquid Microthrusters (VLMs). Compared to cold/hot gas micro-thrusters, VLMs can store the propellant in low pressure and light weight fuel tank, but they will consume more electric power due to the evaporation process. The first development of the VLMs dates back to the Mueller's studies ([14, 15, 16]), who first manufactured a silicon-based MEMS device, characterized the heat losses in relation

to the packaging, and evaluated the influence of feeding pressure on the vaporization process. Later, different configurations ([17], [18], [19], [20],[21], [22] and [12]), materials and manufacturing technologies ([23] and [24]) have been investigated, as described by Gao et al. [25].

The overall numerical analysis of the flow inside a VLM is usually made difficult by the strong coupling of the supersonic flow inside the micronozzle with the flow behavior into the heating chamber. They have always been studied separately focusing on the main specific issues affecting the performance of this kind of microthrusters:

- the growth of the viscous boundary layer inside planar micronozzles, enhanced by the micro-scale and the rarefied gas condition;
- the expansion of non-equilibrium two-phase vapor flow into the micronozzle;
- the establishment of flow boiling instabilities inside the microchannels of the heating chamber.

Bayt and Breuer [26] first conducted 2D numerical simulations on micronozzles for a cold gas microthruster and concluded that the growth of the subsonic boundary layer reduced the thrust efficiency due to the reduction of the actual cross section at the nozzle exit. Other researchers ([27, 28], [29] and more recently [30]), numerically investigated novel two-depth geometries and conventional planar configuration with half-angle of the expander equal to 30° able to mitigate the viscous losses inside micronozzles. In micronozzles the continuum assumption and the no slip condition at walls are easily violated due to a non-negligible degree of gas rarefaction which determines the mechanisms of interaction between gas-gas molecules and solid wall-gas molecules. In general, two different regimes could establish based on the entity of the Knudsen number: the slip flow regime ($0.01 < Kn < 0.1$) or the transitional flow regime ($0.1 < Kn < 10$). In the first regime, the Navier-Stokes equations are still valid when used in combination with partial slip models at walls ([31], [32]).

Instead, in the transitional flow regime, gas kinetic schemes such as Direct Simulation Monte Carlo (DSMC) [33] are required, as in [34] and [35]. Liu et al. [36] demonstrated that the continuum method with slip boundary conditions provided a good estimation of the boundary layer inside the nozzle, albeit in the nozzle exit lip region the DSMC methods performed better due to the rapid gas expansion and the enhanced rarefaction effects. About the micro flow boiling inside microchannels, several numerical models succeeded in well reproducing the nucleation and the growth of the vapor bubble, and the bubble-to-slug transition in a single microchannel (e.g. [37] and [38]). However, nowadays the numerical modeling of micro flow boiling inside complex geometries still represents a challenge due to the strong multiphysics involving microfluidics, phase change and transport phenomena, bubble nucleation, as well as the interaction between the controlled heater and the solid structures.

Based on the complexity of CFD computations highlighted above, a simplified one dimensional modeling that is able to predict the propulsive performance and couple the heating process inside the heating chamber with the flow expansion into the micronozzle, will provide important benefit to the VLM design process. There is few literature on this subject. Specifically, Maurya et al. [39] first proposed a simple theoretical model based on the ideal rocket theory, and introduced an approximated thermal model to estimate the chamber temperature as a function of the heater power. Based on the Maurya's model, Bidabadi et al. [40] developed a new simplified theoretical model which improved the analysis of the heating process in the vaporizing liquid microthruster. Recently, Silva et al [41] proposed an analytical model of key parameters of a VLM which was applied to the attitude control of a picosatellite equipped with four microthrusters.

All of the previously cited works based on ideal flow assumption, and none of them coupled the boiling flow model into the heating chamber to a real nozzle model. The present work proposes a novel one-dimensional analytical modeling of VLM composed of a microchannels system. It implements an iterative coupled approach, and semi-empirical relations to reproduce the real behavior

of the flow. In particular, the steady-state behavior of the two-phase flow inside microchannels is predicted by introducing the empirical relations found by Tibiriçá et al.[42]. Instead, the Ideal Rocket Theory (IRT) allows for the estimation of the ideal performance of the microthruster. Hence, the viscous losses owing to the boundary layer growth are computed in terms of losses of mass flow rate and exit velocity. The former are introduced by estimating the discharge coefficient C_d from the semi-empirical relation by Kuluva and Hosack [43]. The exit velocity losses are analytically derived from the reduction of the momentum, based on the difference between the inviscid and the viscous velocities inside the boundary layer developed over the inner wall of the micronozzle [30]. As a result, the velocity losses depend on the compressible boundary layer thicknesses, which are related to the incompressible boundary layer thicknesses by means of the relations proposed by Whitfield [44]. The I_{sp}-efficiency η_v is thus obtained, leading to the computation of the real nozzle performance. The analytical model was applied to the performance analysis of a MEMS-based VLM composed of a rectangular inlet chamber, a set of parallel microchannels as heating chamber, and a planar convergent-divergent micronozzle. The accuracy of the novel 1D model was evaluated by comparing its performance predictions with those derived from a 2D CFD investigation of the viscous flow inside the micronozzle. For the purpose, the continuum NS flow in partial slip regime was supposed due to a maximum Knudsen number less than 0.1 inside the micronozzle. Different operating conditions were simulated resulting from the one dimensional estimation of the flow state at the microchannels exit. Finally, a further 3D CFD analysis at one single on design operating condition was conducted in order to depict the influence of the micronozzle depth on the boundary layer growth, and compare the extent of the viscous losses with the one predicted by the proposed 1D model.

2. Device configuration and test conditions

The Vaporizing Liquid Microthruster consists of three parts: the inlet chamber or plenum through which the propellant is fed, the heating chamber where the propellant is vaporized, and the convergent-divergent micronozzle, which accelerates the superheated vapor flow to supersonic velocities. The heating chamber is composed of micro-channels to be designed by considering the maximization of the heat transfer coefficient, the reduction of the pressure losses and the control of the boiling instabilities.

In particular, the VLM developed by Cen et al. [22] was analyzed, whose experimental conditions and the corresponding data were used as reference for the validation of the proposed 1D model. As shown in Fig. 1, the device has a planar geometry with depth of 120×10^{-6} m, and it consists of a rectangular plenum upstream, followed by a heating chamber composed of nine parallel microchannels and a convergent-divergent planar nozzle having a throat width of 150×10^{-6} m. The thruster is fabricated in silicon, and the temperature on

Table 1: Microthruster geometry [22].

Region	**Characteristics**
Inlet chamber	2000 µm × 4000 µm × 120 µm
Heating chamber	1120 µm × 6000 µm × 120 µm
composed of 9 microchannels	80 µm width
and 8 separators	50 µm width
Micronozzle	
inlet cross section	1120 µm × 120 µm
throat cross section	150 µm × 120 µm
exit cross section	1760 µm × 120 µm
convergent angle, α_{conv}	45°
divergent angle, α_{div}	15°

the inner walls T_w is supposed to be uniformly distributed due to high thermal conductivity of the silicon. The heating process begins into the plenum at

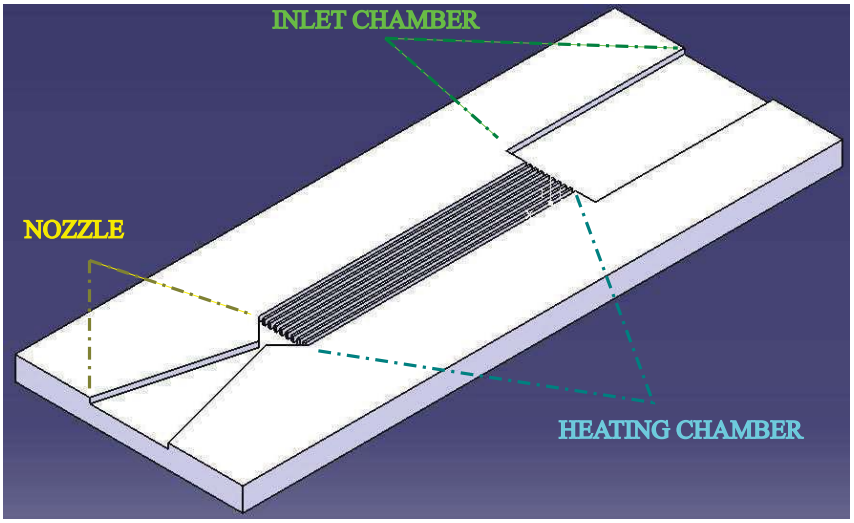

Figure 1: Graphical representation of the VLM.

the end of which the flow experiences a cross section variation entering the microchannels. According to [45], water is used as propellant because it leads to high specific impulse and velocity increment ΔV of the spacecraft compensating the drawback of the power consumption.

The test conditions were chosen based on the phase state diagram experimentally retrieved by Cen [22] and reported in Fig. 2. A preliminary analysis pointed out that the proposed 1D analytical model well performs in on-design operating conditions corresponding to the full evaporation region. Conversely, in off-design condition the accuracy of the 1D model reduced and the performances were predicted with a maximum error region of about 13%. In fact, Cen [22] experimentally observed losses of performance when the microthruster operated into the two-phase flow region, due to the increasing influence of dissipative and rapid condensation phenomena occurring during the expansion process into the micronozzle. Consequently, for the present work the test cases (black circles in Fig. 2) were arbitrarily chosen at three different wall temperatures falling in the full evaporation region, which is lower bounded by the saturated vapor curve (blue line in Fig. 2). The full set of test cases and the corresponding initial

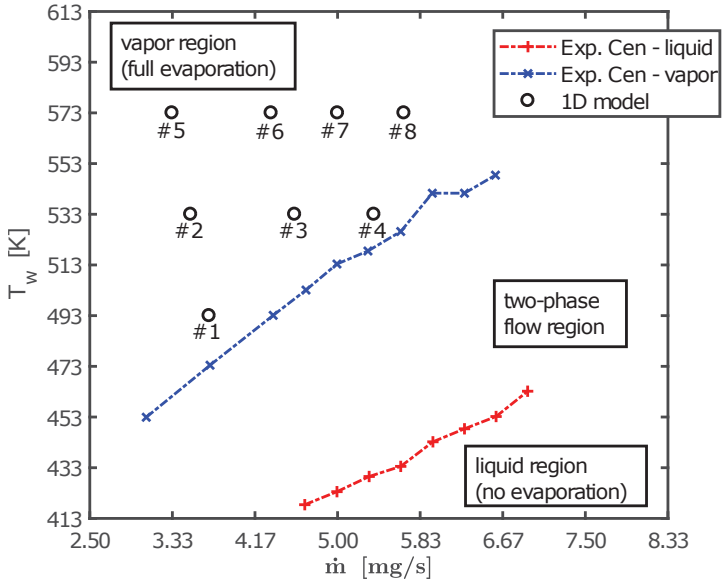

Figure 2: Phase state diagram of the fluid at the exit of the micronozzle. The wall temperature T_w is on the y-axis, and the mass flow rate $\dot{m}$ is on the x-axis. Black circles refer to the test cases denoted by the corresponding number. The saturated liquid curve (red line) and the saturated vapor curve (blue line) correspond to the experimental observations found by Cen et al. [22].

conditions, are reported in Tab. 2.

Table 2: Analytical model investigations: test matrix and operating conditions, where $p_{0,inlet}$ is the inlet total pressure.

Test Case Number	$\mathbf{T_w}$, [K]	$\mathbf{p_{0,inlet}}$, [Pa]	$\dot{\mathbf{m}}$, [mg/s]
#1	493	1.5×10^5	3.70
#2	533	1.5×10^5	3.52
#3	533	1.9×10^5	4.57
#4	533	2.2×10^5	5.37
#5	573	1.48×10^5	3.33
#6	573	1.89×10^5	4.33
#7	573	2.18×10^5	5.00
#8	573	2.41×10^5	5.67

3. Quasi-one-dimensional analytic model

The proposed analytical model sequentially solves the two-phase flow into inlet plenum and microchannels, and the gas flow region inside the micronozzle, as showed in the schematic of Fig. 3. In particular, the modeling of the heating

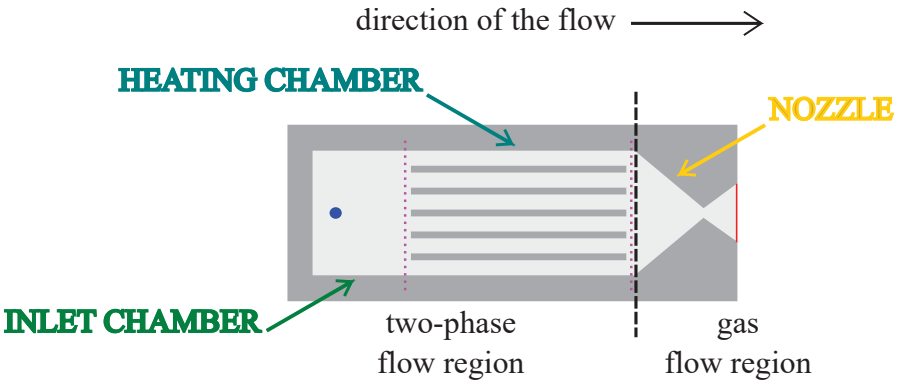

Figure 3: 2D schematic of the working principle of a VLM.

process into the heating chamber and the expansion process into the micronozzle are coupled each other. In fact, the former determines the flow conditions at the micronozzle entrance, while the second one points to estimate the thruster performance taking into account the mass flow rate loss caused by the boundary layer growth inside the micronozzle.

3.1. Two-phase flow region: inlet plenum and heating chamber

A one dimensional steady-state boiling model describes the behavior of the liquid-vapor flow inside the inlet and the heating chambers of the microthruster. As highlighted in Fig. 3, the heating process begins into the inlet chamber at the end of which the flow experiences a cross section variation when it enters the microchannels region. By assuming the hypothesis of thin film flow [46] and the 1D approximation, the following simplifications are made:

- the fluid is Newtonian;
- the fluid properties are averaged over both the height and the width of the flow;
- no slip condition between fluid and walls;
- inertia and other body forces such as the gravity, are supposed negligible compared to pressure and viscous forces, so that the velocity changes result instantaneous.

Furthermore, the properties of the liquid-vapor mixture are determined by means of the toolbox CoolProp [47]. In particular, all properties of the two-phase flow are averaged by supposing the homogeneous mixture of liquid and vapor in thermodynamic equilibrium. Consequently, as evinced in Eq. (1), the generic mixture property $g(\cdot)$, marked by the subscript m, is function of the vapor quality x, and the corresponding saturated properties of liquid and vapor phases, which are denoted by the subscripts l and v respectively:

$$g_m(\cdot) = x\ g_v(\cdot) + (1 - x)\ g_l(\cdot) \tag{1}$$

The resulting set of governing equations are represented by Eqs. (2), (3) and (4), which respectively describe the balance of mass, momentum and energy at each grid step Δs, as follows:

$$\dot{m} = \rho_m u A_{cs} \tag{2}$$

$$\Delta p = -u \frac{12 \mu_m}{Z_{ch}^2} \Delta s \tag{3}$$

$$\Delta H = \dot{Q} \Delta t = \dot{q} \; P_{cs} \; \Delta s = \left[h_b (T_w - T) \right] \; P_{cs} \; \Delta s \tag{4}$$

In the equations above, the time step is $\Delta t = \frac{\Delta s}{u}$, ΔH is variation of the total enthalpy of the flow, ρ_m and μ_m are the density and the dynamic viscosity of the mixture,while Z_{ch} is the height of the channels, which also corresponds to the depth of the entire thruster. Moreover, A_{cs} is the area of the cross section, $\dot{Q}$ is the heat power exchanged between the fluid and the silicon walls and P_{cs} is the perimeter of the cross section. The heat flux $\dot{q}$ is related to the convective heat exchange driven by the heat transfer coefficient $h_b = Nu \frac{\kappa_{cond}}{D_h}$, where κ_{cond} is the local thermal conductivity coefficient of the fluid and D_h is the hydraulic diameter. Instead, the Nusselt number Nu is locally estimated based on the empirical correlations extrapolated by Tibiriçá et al. [42].

The heat transfer process is influenced by the establishment of the dry-out condition $x_{d/o}$ as reported in Eq. (5), which imposes a limit above which the behavior of the saturated liquid-vapor mixture approaches the dry vapor state:

$$x_{d/o} = \min(x_{incip}, x_{crit}, x_{dry,max}) \tag{5}$$

where $x_{dry,max}$ is an upper limit set equal to 0.95 as suggested by [42], x_{incip} is the incipient dry-out vapor quality estimated as:

$$x_{incip} = 0.6827 \; Eo^{0.07395} \; X_{\rho}^{0.07149} \; Bo^{0.04786} \; (1 - x_{TD})^{-0.3378} \tag{6}$$

In Eq. (6), x_{TD} is the thermodynamic vapor quality of the water-steam mixture at the entrance of the inlet chamber, and x_{crit} is the vapor quality corresponding

to the critical heat flux condition (CHF), resulting from:

$$x_{crit} = 4\ Bo \left[4.124\ Bo\ We^{0.1625}\ X_{\rho}^{0.05981}\ La^{0.07142}\ (1-x_{TD})^{-0.8809} \right]^{-1.4632} + x_{TD} \tag{7}$$

Finally, the local heat transfer coefficient is estimated as in Eq. (8):

$$h_b = \begin{cases} \frac{Nu(x)\ \kappa_{cond}}{D_h} & \text{if } x < x_{d/o} \\ \frac{Nu(x)\ \kappa_{cond}}{D_h} - 0.5 \left[\frac{Nu(x)\ \kappa_{cond}}{D_h} - h_{b,DB} \right] \frac{(x-x_{d/o})}{(1-x_{d/o})} & \text{if } x \geq x_{d/o} \end{cases} \tag{8}$$

Instead, the local Nusselt number and the Dittus-Boelter superheated vapor relation are defined in Eqs. (9) and (10):

$$Nu(x) = \begin{cases} 0.68\ Pr^{0.5414}\ La^{0.1942}\ Re^{0.5873}\ (1-x)^{-0.2446}\ Bo^{0.3544} & \text{if } x < x_{d/o} \\ 0.68\ Pr^{0.5414}\ La^{0.1942}\ Re^{0.5873}\ (1-x_{d/o})^{-0.2446}\ Bo^{0.3544} & \text{if } x \geq x_{d/o} \end{cases} \tag{9}$$

$$h_{b,DB} = 0.023\ \frac{\kappa_{v,cond}}{D_h}\ Re_v^{0.8}\ Pr_v^{1/3} \tag{10}$$

where Re_v and Pr_v respectively are the local Reynolds and Prandtl numbers of the vapor phase. The operational range of validity of the experimental correlations by [42] is reported in Tab. 3.

3.2. Single-phase vapor flow region: the micronozzle

The analysis of the vapor flow through the micronozzle is based on the ideal rocket theory (IRT) [48], which is improved to take into account viscous losses. Based on the chocked flow conditions, the maximum mass flow rate $\dot{m}_{IRT}$ is expressed as a function of the stagnation pressure p_0 and temperature T_0 at the exit of microchannels, and the area at the throat section A^*, as follows:

$$\dot{m}_{IRT} = \Gamma_{VDK} \frac{p_0 A^*}{\sqrt{R_{gas} T_0}} \tag{11}$$

where R_{gas} is specific gas constant, $\gamma = \frac{c_p}{c_v}$ is the specific heat ratio of the propellant and Γ_{VDK} is the Vanderkerchoff factor. The Mach number at the

Table 3: Operational ranges of validity of the experimental correlations by [42].

Quantity	**Range of validity**
Fluids	water, R12, R22, R123, R134a, R236fa, R245fa, R1234ze(E), R1234yf, R744 (Carbon Dioxide), R290 (Propane), R410a, R600a and nitrogen
We^*	$[1 \times 10^{-1} \div 2 \times 10^5]$
La^*	$[46\,600 \div 3\,131\,000]$
Re^*	$[120 \div 14\,600]$
Bo^*	$[4.6 \times 10^{-5} \div 2.5 \times 10^{-3}]$
Pr^*	$[0.9 \div 6.6]$
${x_{TD}}^*$	$[-0.6 \div 0.15]$
$\frac{\texttt{channel length}}{\texttt{channel diameter}}$	$[20 \div 500]$
X_ρ	$[6.5 \div 129\,000]$

* evaluated at the entrance of the inlet chamber.

exit section is determined by means of the relation (12):

$$\frac{A_{exit}}{A^*} = \frac{1}{M_{exit}} \left\{ \left(\frac{2}{\gamma + 1} \right) \left[1 + 0.5\,(\gamma - 1)\,M_{exit}^2 \right] \right\}^{\frac{(\gamma+1)}{2(\gamma-1)}} \tag{12}$$

The exhaust velocity is calculated by means of Eq. (13).

$$u_{exit,IRT} = \sqrt{\frac{2\gamma R_{gas} T_0}{\gamma - 1} \left[1 - \left(\frac{p_{exit}}{p_0} \right)^{\frac{(\gamma-1)}{\gamma}} \right]} \tag{13}$$

Finally, the ideal performance of the microthruster can be predicted in terms of thrust and specific impulse, as highlighted in Eqs. (14) and (15),

$$F_{IRT} = F_{j,IRT} + F_{p,IRT} = \dot{m}_{IRT}\; u_{exit,IRT} + (p_{exit,IRT} - p_{amb})\; A_{exit} \tag{14}$$

$$I_{sp,IRT} = \frac{F_{IRT}}{\dot{m}_{IRT}\; g_0} = \frac{u_{eff}}{g_0} \tag{15}$$

where the subscripts j and p denote the momentum thrust and the pressure thrust respectively, and u_{eff} is the effective exhaust velocity which takes into account both thrust terms.

Due to the micro-scale of the flow, the performance of a microthruster is strongly affected by the establishment of the boundary layer at the nozzle throat and along the divergent section. As a result, the actual thrust decreases due to losses of both mass flow rate and exit velocity, as in Eq. (16):

$$F_{act} = \dot{m}_{act} u_{act} = (C_d\ \dot{m}_{IRT})\ (\eta_u\ u_{IRT}) = (C_d \eta_u)\ \dot{m}_{IRT} u_{IRT} = \xi_n F_{IRT} \quad (16)$$

where C_d is the discharge coefficient, η_u is the I_{sp}-efficiency, and $\xi_n = C_d\ \eta_u$ defines the global propulsive efficiency, better known as nozzle quality. As highlighted in Eq. (16), the nozzle quality quantifies the total performance losses due to the boundary layer thickness inside the micronozzle.

Discharge Coefficient model, C_d. Based on the work by Kuluva and Hosack [43], the discharge coefficient C_d is related to the geometry of the nozzle throat, the propellant and the Reynolds number at the throat section Re^* by means of Eq. (17):

$$C_d = C_d\left(\frac{r_c}{0.5\ W^*}, \gamma, Re^*\right) = \left[\frac{r_c + 0.05\ (0.5W^*)}{r_c + 0.75\ (0.5W^*)}\right]^{0.019} \left\{1 - \left[\frac{r_c + 0.10\ (0.5W^*)}{(0.5W^*)}\right]^{0.21} \left(\frac{1}{Re^*}\right)^{0.5} f(\gamma)\right\} \quad (17)$$

where r_c and W^* are the radius of curvature and the width of the throat, and $f(\gamma) \simeq 0.97 + 0.86\gamma$. As specified in [43], Eq. (17) estimates the discharge coefficient as the contraction of the throat area owing to the growth of the viscous boundary layer thickness along the inner walls. The operational range of validity of the correlation (17) is $0 \leq r_c/W^* \leq 20$ and $50 \leq Re^* \leq 1 \times 10^5$.

I_{sp}-efficiency, η_u. The difference between the inviscid and the viscous velocity inside the boundary layer leads to a reduction of the momentum ΔJ. Similarly to Sokolov and Chernyshov [30], ΔJ has been derived for a planar nozzle as a function of the compressible displacement δ^* and the momentum thicknesses θ:

$$\Delta J = \dot{m}_{act} u_{exit,IRT} \left(\frac{2\delta^*}{W_{exit}}\right) \left(1 + \frac{\theta}{\delta^*}\right) = \dot{m}_{act}\ \Delta u_{exit} \quad (18)$$

Consequently, the I_{sp}-efficiency is expressed as follows:

$$\eta_u = \frac{u_{exit,act}}{u_{exit,IRT}} = \frac{u_{exit,IRT} - \Delta u_{exit}}{u_{exit,IRT}} = 1 - \left(\frac{2\delta^*}{W_{exit}}\right)\left(1 + \frac{\theta}{\delta^*}\right) \tag{19}$$

δ^* and θ depend on the Reynolds number and the Mach number at the exit, namely Re_{exit} and M_{exit}. As proposed by Whitfield [44], they are related to the incompressible thicknesses by means of the following relations:

$$S_{\delta^*} = \frac{\delta^*}{\theta} = \bar{S}\,(1 + 0.113M_{exit}^2) + 0.290M_{exit}^2 \tag{20}$$

$$\theta = \bar{\theta}\left\{1 - \frac{0.92M_{exit}^2}{7.09 + M_{exit}^2}\tanh[1.49(\bar{S} - 0.9)]\right\} \tag{21}$$

where S_{δ^*} is the compressible shape factor, $\bar{\delta^*}$ and $\bar{\theta}$ are respectively the incompressible displacement and momentum thicknesses, and $\bar{S} = \bar{\delta^*}/\bar{\theta}$ is the incompressible shape factor. The Eqs. (22), (23) and (24) proposed by Çengel and Cimbala [49] for turbulent flows are used to estimate $\bar{\theta}$ and $\bar{S}$, as follows:

$$\frac{\bar{\delta^*}}{L} = \frac{0.048}{Re_{exit}^{1/5}} \tag{22}$$

$$\frac{\bar{\theta}}{L} = \frac{0.037}{Re_{exit}^{1/5}} \tag{23}$$

$$\bar{S} = \frac{0.048}{0.037} = 1.2973 \tag{24}$$

where L is the slanted length of the expander.

3.3. Solution procedure

The solution procedure of the proposed model is iterative and based on a two-cycle criterion, as highlighted in Fig. 4. In particular, the first cycle forwardly solves the two-phase flow from the entrance to the exit of the heating region. The initialization of the mass flow rate is based on the hypothesis of chocked micronozzle (Eq. (11)), using T_w and p_i. The Nusselt number is constant, equal to 4.96 as suggested by Bejan [50]. By estimating the error between the new mass flow rate with the old one, the mass flow rate is corrected before to start a new computational loop, until convergence is reached based on a residual tolerance of 0.01. The convergence on the first cycle leads to the estimation of

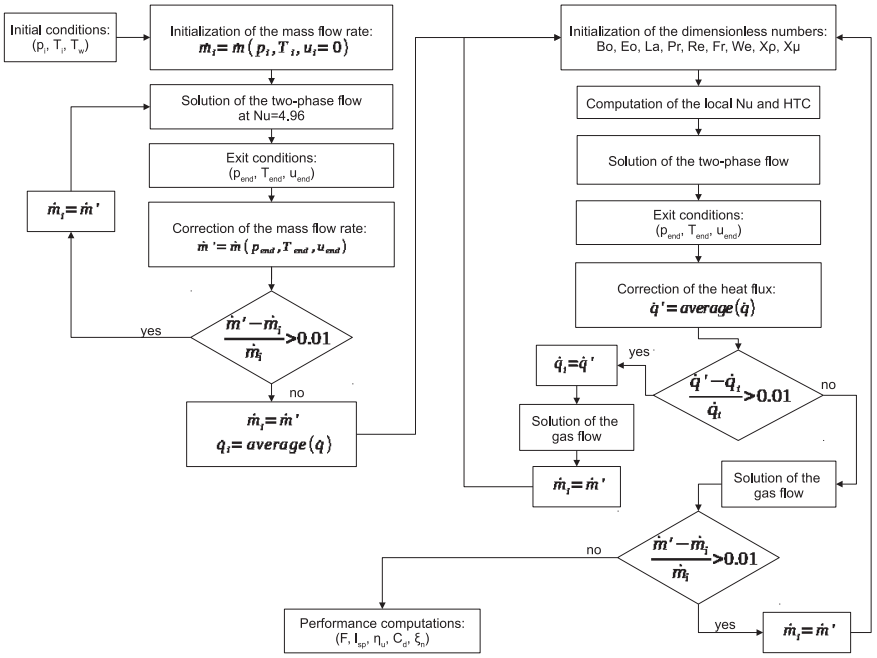

Figure 4: Solution procedure of the analytical model.

the average heat flux $\dot{q}_0$ required for the initialization of the boiling number Bo and the other dimensionless numbers used in the experimental correlation by Tibiriçá et al.[42]. This ensures stability in the solution of the second and most important cycle, which is constructed using the empirical relations presented in the previous section. Concerning the second cycle, the two-phase flow inside the heating region is first solved based on the local estimation of the Nusselt number. Hence, a new value of the average heat flux is estimated and a correction step is introduced on it, based on a residual tolerance of 0.01. Therefore, the solution of the gas flow inside the micronozzle is computed starting from the fluid state predicted at the exit of the microchannel. Finally, the microthruster performances are estimated based on the IRT and the computation of the viscous losses. The latter leads to the corrected mass flow rate at the end of each cycle loop. Thus, similarly to the first cycle, the mass flow rate correction is performed based on a residual tolerance of 0.01.

4. CFD modeling of the gas flow

4.1. The numerical solver

The 2D and 3D simulations of the gas flow through the micronozzle were performed by using the open source CFD toolbox OpenFOAM© Version 3.0.1, based on a Finite Volume formulation. The density-based solver *rhoCentralFoam* [51] was used for computations. In simulations, the Reynolds number of the vapor flow along the mid axis of the nozzle ranged from about 3150 at the throat section up to about 600 at the exit section. Thus, the compressible Navier-Stokes (NS) equations were solved in combination with the laminar flow approximation in reference to the turbulence modeling.

Concerning numerical schemes, the central upwind scheme of Kurganov and Tadmor [52] was used for the flux terms and the Total Variation Diminishing (TVD) van Leer limiter [53] for interpolation. Moreover, the Gauss linear scheme was used for both the divergence, the gradient and the Laplacian operators. Time derivatives were computed with the first order, bounded and

implicit Euler scheme. The time step was determined based on a maximum Courant number Co_{max} of 0.2. In particular, the viscous governing equations were solved using a Preconditioned Conjugate Gradient/Diagonal Incomplete Cholesky scheme with a residual tolerance of 1×10^{-8}, while the inviscid equations of momentum and energy were explicitly solved by means of a Gauss-Siedel Smooth solver with a residual tolerance of 1×10^{-10}. In order to guarantee numerical stability during the transient, each simulation was split into three temporal intervals, i.e. $[0 - 0.5 \times 10^{-4}]$ s, $[0.5 \times 10^{-4} - 1 \times 10^{-4}]$ s and $[1 \times 10^{-4} - 3 \times 10^{-4}]$ s, and the mass flow rate was increased at the beginning of each step. The establishment of the steady state regime was ensured by monitoring the Mach number at mid point of nozzle exit.

4.2. Computational domain, numerical setup and boundary conditions (BCs)

The geometry of the micronozzle was based on the microthruster developed by Cen et al. [22] and summarized in Tab. 1. A radius of curvature equal to 75 µm characterized the throat section, while at the inlet eight equivalent microchannels of 90 µm width preserved the actual cross section area, in combination with a mixing region of 180 µm length before the entrance into the convergent region. Both 2D and 3D simulations were performed, and the corresponding computational domains are shown in Fig. 6(a) and (b), which considered the symmetry of the micronozzle.

The 2D domain extended $15W_{exit}$ downstream and $6.5W_{exit}$ upward, where W_{exit} is the width of the exit section, while the 3D mesh had an outer domain extended $5W_{exit}$ upward, $10W_{exit}$ downstream and $50Z_{ch}$ sideways, where Z_{ch} represents the nozzle depth. Water vapor was assumed as propellant, for which polynomial laws were used for the computation of the dynamic viscosity and the specific heat capacity at constant pressure, in combination with the Peng Robinson equation of state [54]. The CFD model solved the vapor flow into the nozzle by supposing a gas expansion process without condensation phenomena, in accordance with the full evaporation condition as discussed in the previous section 2.

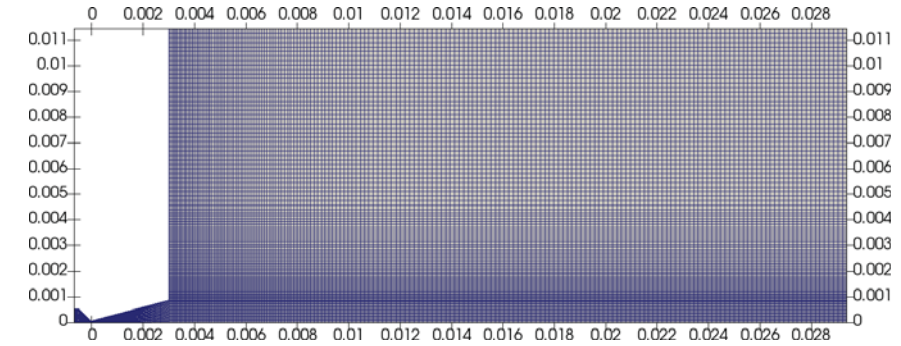

Figure 5: 2D computational domain: (a) global view; (b) focused view. Units are in metre, [m].

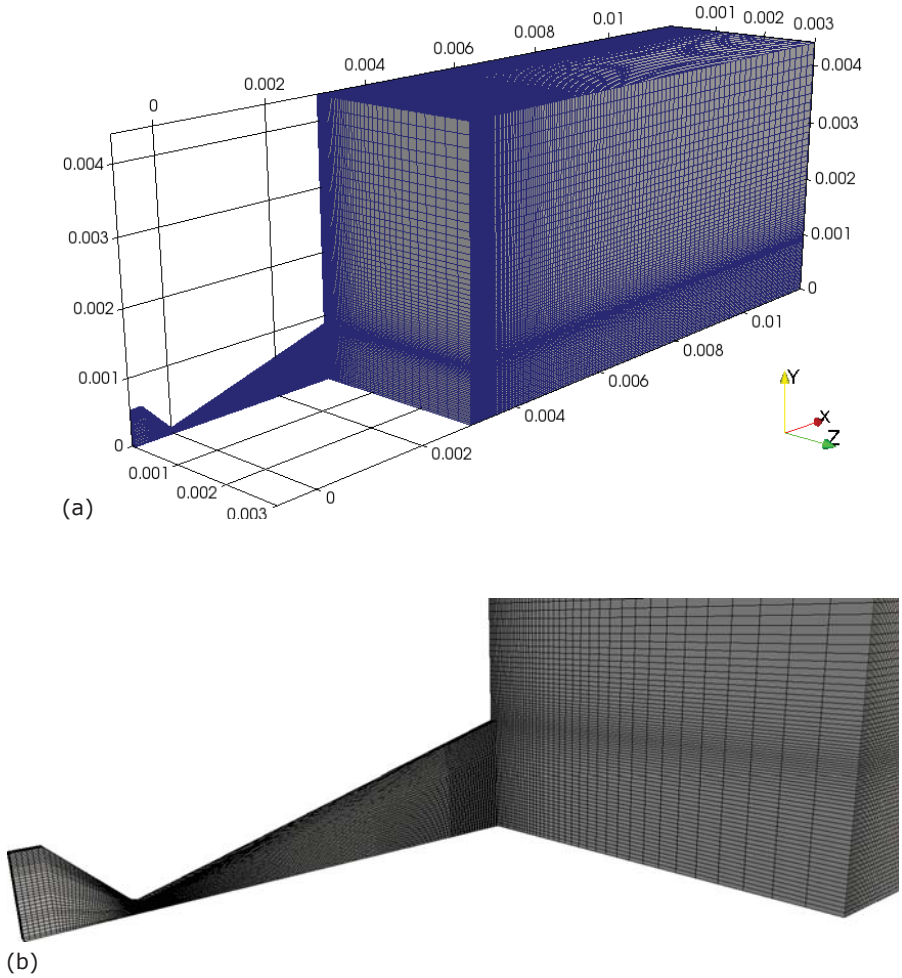

Figure 6: 3D computational domain: (a) global view; (b) focused view. Units are in metre, [m].

Concerning the boundary conditions, simulations were performed by setting the inlet mass flow rate and the static back pressure as reported in Tab. 4. Furthermore, a partial slip boundary condition at walls was used since the max-

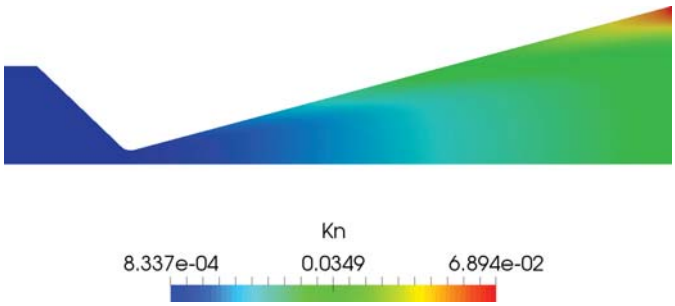

Figure 7: 2D contour of the Knudsen number Kn at $T_{inlet} = 505.58\,\mathrm{K}$ and $\dot{m} = 5 \times 10^{-6}\,\mathrm{kg\,s^{-1}}$.

imum Knudsen number Kn into the divergent was strictly below 1×10^{-1}, as shown in Fig. 7 corresponding to the developed field inside the micronozzle at $T_{inlet} = 505.58\,\mathrm{K}$ and $\dot{m} = 5 \times 10^{-6}\,\mathrm{kg\,s^{-1}}$. In particular, a tangential momentum accommodation coefficient (σ_{TMAC}) of 0.80 was imposed using a first order Maxwell slip model in reference of a generic gas flow on polished silicon microchannels. It is worth to observe that the transitional gas rarefaction regime could occur outside the micronozzle, due to the low-pressure condition. Even if a DSMC approach is valid for all flow regimes, it would requires increasing grid size and time step size as the Knudsen number decreases. Since the computational expense of a proper DSMC simulation scales with Kn^{-4}, it is impossible to use DSMC to an entire micro-nozzle flow. On the other hand, when $Kn < 0.1$, the flow can still be described by continuum Navier-Stokes equations since it is dominated by intermolecular interactions. In addition, the main focus of the present investigation is on the analysis of the supersonic flow inside the micronozzle, and both 2D and 3D simulations aimed to provide a performance analysis for comparisons with respect to the proposed 1D modeling. Hence, a DSMC approach was not considered in favor of a continuum NS model which allowed to reduce the computational cost even though with an accuracy

loss into the jet plume domain.

Each CFD simulation was initialized by setting the mass flow rate and the vapor temperature at the exit of microchannels predicted by the 1D model at the micronozzle inlet, and the back pressure as outlet condition. The whole test matrix and the initial conditions are reported in Tab. 4, which refer to the same heating conditions, i.e. $T_w = 573\,\mathrm{K}$. As a result, the Reynolds number at the throat section ranged between 1550 and 3150. Moreover, the viscous flow at

Table 4: Test matrix of CFD simulations.

Test Case	**Flow type**	$\mathbf{T_{inlet}}$, [K]	$\dot{\mathbf{m}}$, [mg/s]	$\mathbf{p_{outlet}}$, [Pa]	**Slip Condition**
SIM4-2D	2D	520.48	3.33	20	Maxwell, $\sigma_{TMAC} = 0.80$
SIM5-2D	2D	510.32	4.33	20	Maxwell, $\sigma_{TMAC} = 0.80$
SIM5-2Dslip	2D	510.32	4.33	20	Pure Slip
SIM2-2D	2D	505.58	5.00	20	Maxwell, $\sigma_{TMAC} = 0.80$
SIM2-2Dslip	2D	505.58	5.00	20	Pure Slip
SIM2-3D	3D	505.58	5.00	20	Maxwell, $\sigma_{TMAC} = 0.80$
SIM6-2D	2D	501.52	5.67	20	Maxwell, $\sigma_{TMAC} = 0.80$
SIM6-2Dslip	2D	501.52	5.67	20	Pure Slip
SIM7-2D	2D	497.50	6.42	20	Maxwell, $\sigma_{TMAC} = 0.80$

$\dot{m} = 5 \times 10^{-6}\,\mathrm{kg\,s^{-1}}$ was also solved in 3D conditions in order to provide a more detailed insight of the influence of the micronozzle depth Z_{ch} on the boundary layer effects and microthruster's performance.

The analysis of the micronozzle's behavior considered a numerical discharge

coefficient computed as follows:

$$C_{d,CFD} = \frac{\dot{m}}{\dot{m}_{IRT}} \tag{25}$$

where $\dot{m}_{IRT}$ is defined in Eq. (11) by using the average total pressure at the inlet predicted by CFD simulations. The estimation of the I_{sp}-efficiency was performed by comparing the thrust force (F) resulting from the use of the Maxwellian slip (SIM2-2D, SIM5-2D and SIM6-2D in Tab. 4), with the one obtained by setting the pure slip condition at wall ($F_{pureSlip}$) at the same operating conditions (SIM2-2Dslip, SIM5-2Dslip and SIM6-2Dslip in Tab. 4), as follows:

$$\eta_{v,CFD} = \frac{F}{F_{pureSlip}} \tag{26}$$

In accordance with Cen [22], the thrust force was estimated by means of cell-based integration of the local jet thrust over the section normal to the axial direction and placed at 2 mm downstream the nozzle exit. Hence, the specific impulse was computed by definition as:

$$I_{sp,CFD} = \frac{F}{\dot{m}\, g_0} \tag{27}$$

where $g_0 \cong 9.81\,\mathrm{m\,s^{-2}}$ is the gravitational acceleration at sea level. Finally, the entity of the boundary layer was evaluated by computing at the exit section the displacement and the momentum thicknesses, δ^* and θ respectively, as follows:

$$\delta^* = \int_0^\infty \left[1 - \frac{\rho u_x}{(\rho u_x)_\infty}\right] dy \tag{28}$$

$$\theta = \int_0^\infty \frac{\rho u_x}{(\rho u_x)_\infty}\left[1 - \left(\frac{u_x}{u_{x,\infty}}\right)\right] dy \tag{29}$$

where the subscript x denotes the axial direction of the flow, and ∞ denotes the undisturbed flow condition.

4.3. Grid independence study (GIS)

A grid independence study (GIS) was conducted based on the analysis of water vapor flow at $\dot{m} = 5\,\mathrm{mg\,s^{-1}}$ and $p_{outlet} = 20\,\mathrm{Pa}$, corresponding to a Reynolds number at the throat section equal to about 2420. The grid sensitivity was evaluated by comparing the Mach number profile at the exit section

M_{exit} obtained using three meshes, differently refined inside the micronozzle as reported in Tab. 5.

Table 5: Grid Independence Study for the 2D mesh: characteristics of the mesh refinements.

Test Case	**Refinement Level**	**Edge Node Number**[a]	**Average Spacing**[a] [µm]	**Cell Number**	θ^{a} [µm]
SIM1-2D	Fine	36	48.89	35690	28.79
SIM2-2D	Intermediate	21	83.81	23931	28.68
SIM3-2D	Coarse	13	135.38	17732	27.06

[a] referred to the exit section

The mesh refinement affected mainly the region of the boundary layer, as shown in Fig. 8. In fact, the profiles of the Mach number at the nozzle exit

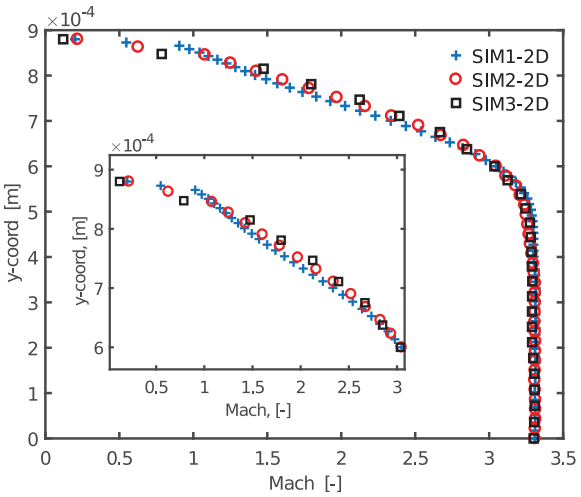

Figure 8: Comparison of the Mach number profile at the exit section: 1) SIM1-2D, fine mesh; 2) SIM2-2D, intermediate mesh; 3) SIM3-2D, coarse mesh.

overlap inside the cold core of the flow, but close to the inner walls of the thruster there is an improvement in results when the refinement level from

coarse (SIM3-2D) to intermediate (SIM1-2D).

In order to accomplish the GIS, the discretization error between two consecutive refinement levels was estimated by computing the grid convergence index (GCI), as suggested by the National Aeronautics and Space Administration [55] research guidelines. The compressible momentum displacement thickness θ was used as a representative parameter, and the average height of cells at the exit section was used as the grid spacing factor. Tab. 6 reports the results. According to the Richardson extrapolation method, GCI_{12} (fine to intermediate refinement error) is smaller than GCI_{23} (intermediate to coarse refinement error). Consequently, the error was estimated to be equal to about 0.035%, corresponding to GCI_{12}.

Table 6: Grid Independence Study for the 2D mesh: GGI parameters.

Test Case	**Grid Spacing**	**GCI parameter**	**CGI** [%]
SIM1-2D	1	28.79	$GCI_{12} = 0.03479$
SIM2-2D	1.7143	28.68	$GCI_{23} = 0.51435$
SIM3-2D	2.7692	27.06	-

The 2D grid independence study led to the choice of the intermediate mesh composed of 23931 cells. Hence, the construction of the 3D mesh, consisting of 516360 cells, was based on the same refinement levels adopted for the 2D domain. However, the external domain was restricted downstream and upward in order to obtain a reduction of the computational cost without loss of accuracy.

5. Results and Discussion

5.1. Quasi-one-dimensional analytic model

The present analytical modeling constitutes a novel design tool of VLMs. In order to underline the improvement of the present model in predicting the heat exchanged between fluid and solid walls, Fig. 9 shows the axial profiles of Nu,

HTC, fluid temperature, static pressure and vapor quality, at $T_w = 573\,\mathrm{K}$ and $\dot{m} = 5 \times 10^{-6}\,\mathrm{kg\,s^{-1}}$. In the figure, s/L_{tot} represents the dimensionless axial coordinate and L_{tot} is the total length of the heating region (i.e the inlet plenum and the heating chamber). The heat flux based model computed a higher Nu and HTC with respect to the constant Nusselt based mode with $Nu = 4.96$ (see Fig. 9(a) and (b)), which resulted in a lower pressure drop and a higher temperature of the vapor at the exit of microchannels (highlighted in Fig. 9(c) and (d)). Furthermore, the heat flux based model exhibited faster evaporation process with respect to the constant Nusselt based model, as evinced in Fig. 9(e). In fact, the heat flux based model estimated the complete evaporation at $s/L_{tot} = 0.34$, while the constant Nusselt based model predicted it at $s/L_{tot} = 0.46$.

As highlighted in Fig 10, at a given wall temperature, the residence time increased as the mass flow rate reduced due to the increased velocity of the flow. This resulted in an improvement of the heating process which produced a stronger superheating of the vapor phase. Furthermore, a linear relationship was found between the electrical power required for the heating process P_r and the mass flow rate $\dot{m}$ at fixed wall temperature was retrieved, as pointed out in Tab. 7. In particular, it was found that as the wall temperature increased, P_r slightly increased and the slope of the linear relation $P_r - \dot{m}$ became steeper.

Based on the predicted flow conditions at the microchannels exit, the performance of the microthruster were estimated by analyzing the supersonic flow into the micronozzle, as shown in Fig. 11 in comparison with experiments by Cen [22]. The good agreement between the 1D model predictions in real flow conditions and experiments demonstrated and confirmed the prediction improvement of the present model with respect to the isentropic solution based on the simplified IRT.

The maximum estimation error was about 7.3% for both thrust force and specific impulse, as shown in Tab. 7.

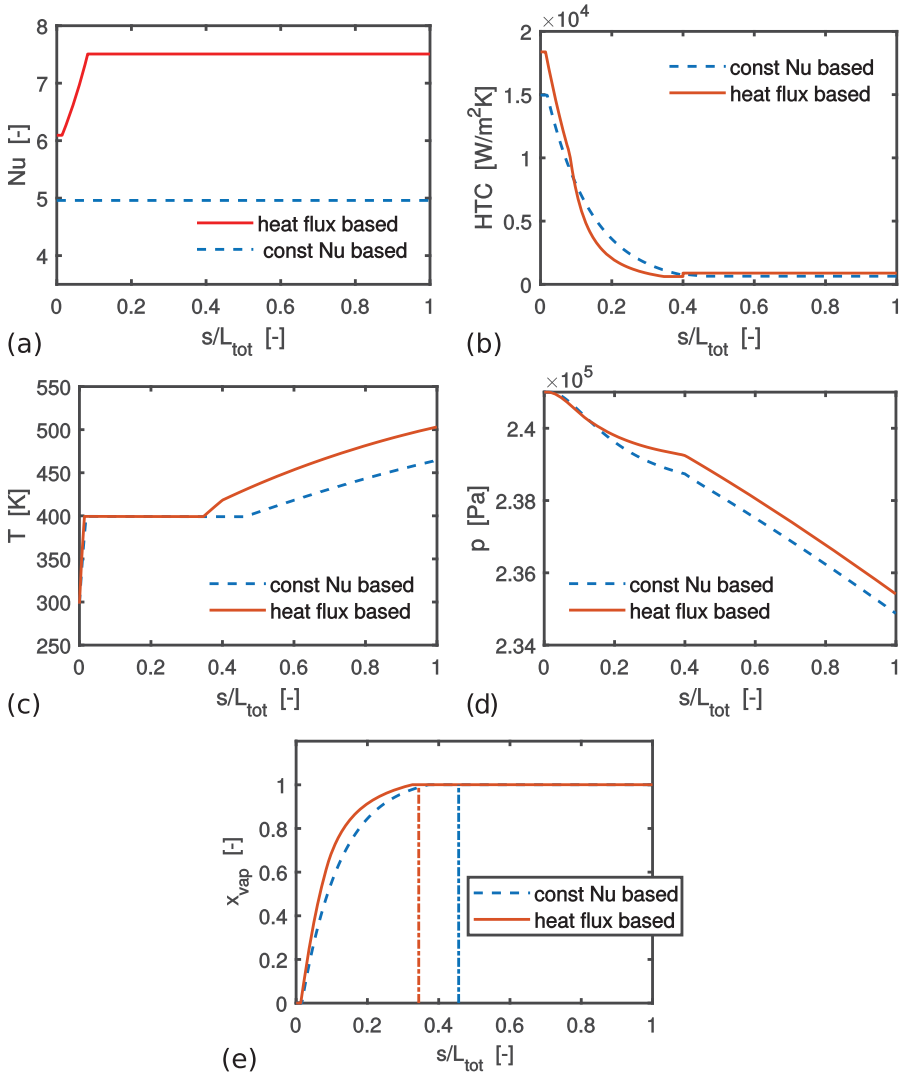

Figure 9: Longitudinal profiles of Nusselt number Nu (a), heat transfer coefficient HTC (b), fluid temperature T (c), static pressure p (d) and vapor quality x_{vap} (e), at $T_w = 573\,\mathrm{K}$ and $\dot{m} = 5.00\,\mathrm{mg\,s^{-1}}$ (TEST #7). Comparison between the constant Nusselt based model and the heat flux based model. L_{tot} is the total length of the heating region (inlet plenum + heating chamber).

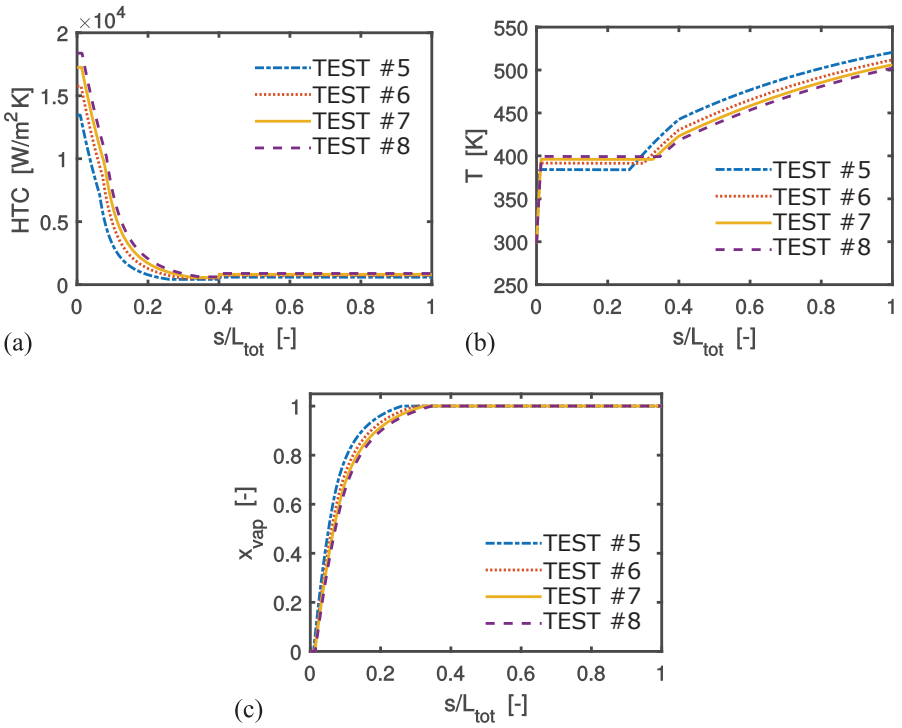

Figure 10: Comparison of the longitudinal profiles of heat transfer coefficient HTC (a), fluid temperature T (b), and vapor quality x_{vap} (c), at $T_w = 573\,\mathrm{K}$ and $\dot{m} = 3.33\,\mathrm{mg\,s^{-1}}$ (TEST #5), $\dot{m} = 4.33\,\mathrm{mg\,s^{-1}}$ (TEST #6), $\dot{m} = 5.00\,\mathrm{mg\,s^{-1}}$ (TEST #7) and $\dot{m} = 5.67\,\mathrm{mg\,min^{-1}}$ (TEST #8).

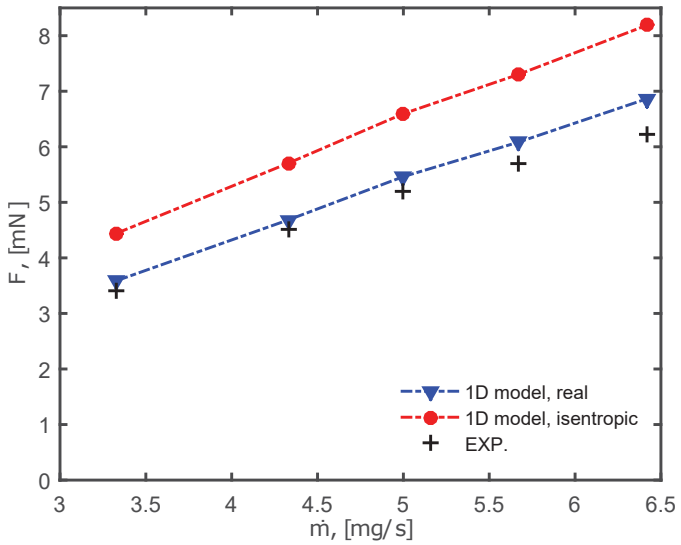

Figure 11: Comparison between 1D model predictions of the thrust force F and experiments (EXP, [22]]) as a function of the mass flow rate $\dot{m}$ at $T_w = 573\,\mathrm{K}$.

Table 7: Comparison between experimental data (EXP, [22]]) and 1D model predictions of electrical power P_r required for evaporation, the thrust force F and specific impulse I_{sp}, for each test case. Err denotes the relative deviation of numerical results from experiments.

Test #	$\mathbf{T_w}$ [K]	$\dot{\mathbf{m}}$ [mg/s]	$P_{r,1D}$ [W]	$\mathbf{F_{1D}}$ [mN]	$\mathbf{F_{EXP}}$ [mN]	$\mathbf{Err_F}$ [%]	$\mathbf{I_{sp,1D}}$ [s]	$\mathbf{I_{sp,EXP}}$ [s]	$\mathbf{Err_{Isp}}$ [%]
#1	493	3.70	9.98	3.66	3.56	+2.9	100.8	96.3	+4.7
#2	533	3.52	9.79	3.66	3.41	+7.3	105.9	98.8	+7.3
#3	533	4.57	12.62	4.72	4.52	+4.6	105.4	100.5	+4.9
#4	533	5.37	14.75	5.53	5.23	+5.7	105.0	98.7	+6.4
#5	573	3.33	9.49	3.59	3.40	+5.6	110.4	103.4	+6.8
#6	573	4.33	12.34	4.68	4.50	+4.1	110.1	105.1	+4.7
#7	573	5.00	14.36	5.46	5.20	+5.1	110.0	106.7	+3.0
#8	573	5.67	15.97	6.08	5.70	+6.7	109.6	102.3	+7.2

5.2. Comparison of 1D model and 2D CFD predictions of the micronozzle flow

The 1D model highlighted the strong impact of the boundary layer growth on the performance of the microthruster. Consequently, a 2D CFD investigation was performed in order to provide a more detailed description of the viscous behavior of the flow inside the micronozzle. Figures 12(a) and (b), show the 2D CFD results in comparison with predictions provided by the improved 1D analytical model. Both models retrieved a similar trend of the global performance

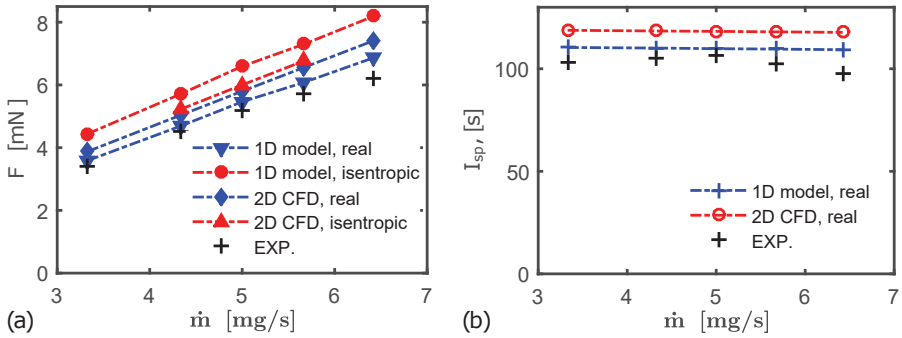

Figure 12: Comparison between 1D model, 2D CFD and experiments (EXP, [22]]) as a function of the mass flow rate $\dot{m}$ at $T_w = 573\,\mathrm{K}$: (a) thrust force F; (b) specific impulse I_{sp}.

as a function of the mass flow rate. However, the 2D CFD model over-predicted both the thrust force and the specific impulse with respect to the analytical model, even though higher boundary layer thicknesses δ^* and θ were estimated at the nozzle exit, as shown in Figs. 13(a) and (b).

The reason of these conflicting findings lies on the different hypotheses and approximations of the analytical and 2D CFD approaches. In fact, the analytical model uses semi-empirical relations (17)-(21) previously reported, which take account of 3D real flow effects at least in part, despite being based on the approximated theory of the flat plate boundary layer. Conversely, 2D CFD computations reproduced the boundary layer growth along the slanted walls of the expander, yet they neglected the influence of the micronozzle depth, as well as non-equilibrium phase-change phenomena occurring into the divergent section of the micronozzle. This is confirmed by comparing the analytical results

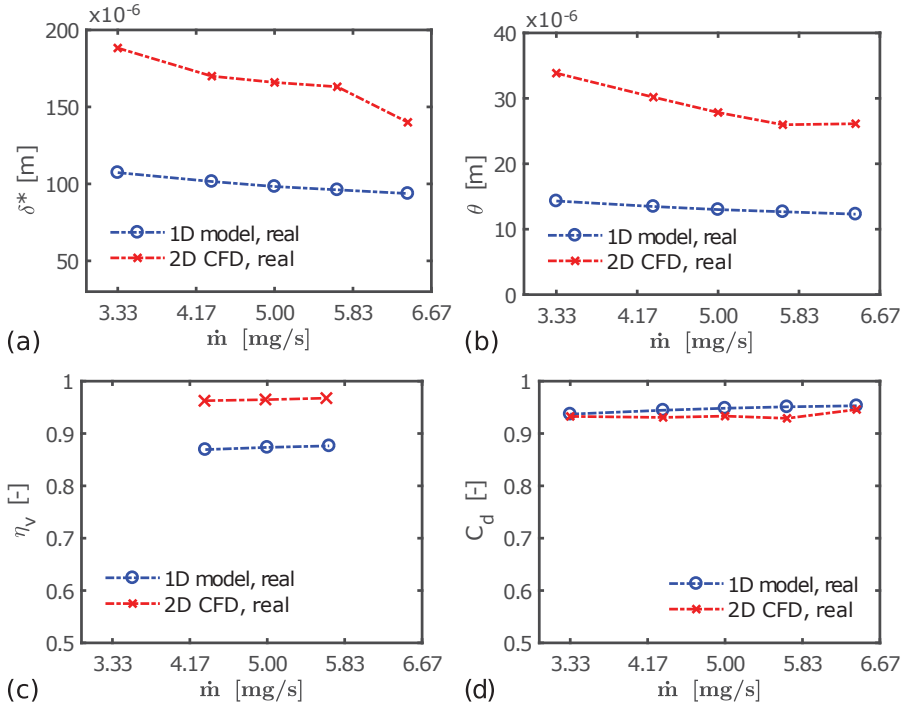

Figure 13: Boundary layer analysis as a function of the mass flow rate $\dot{m}$ at $T_w = 573\,\mathrm{K}$. Comparison between predictions provided by the 2D CFD and the 1D model.

in isentropic flow conditions and the CFD simulations in pure slip regime at walls, whose results well matched each other as shown in Fig. 12. A detailed representation of the 2D boundary layer growth inside the micronozzle is shown in Fig. 14, which compares the contours of the velocity magnitude resulting from the use of the pure slip condition (SIM2-2Dslip) and the Maxwellian slip condition (SIM2-2D).

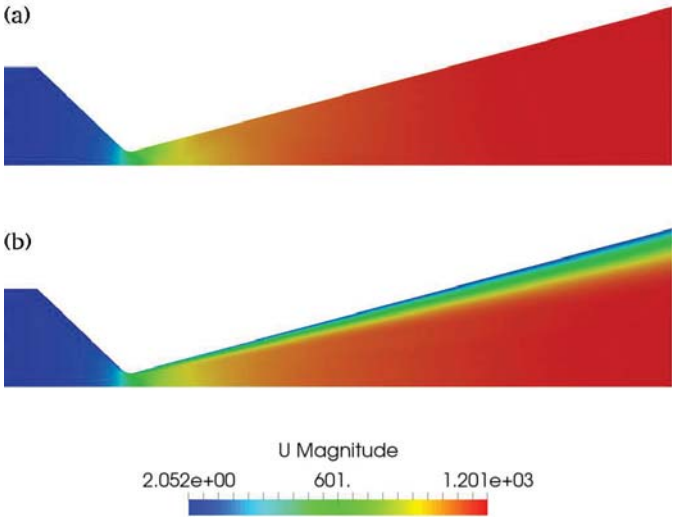

Figure 14: CFD contours of the velocity magnitude $|\mathbf{u}|$: (a) pure slip condition (SIM2-2Dslip); (b) Maxwellian slip condition (SIM2-2D). Units are in metre per second, [m/s].

The influence of the boundary layer on the performance of the micronozzle was evaluated by means of η_v and C_d. The comparison between the viscous and isentropic solutions of both 1D and 2D models highlighted a reduction of the mass flow rate up to about 8%, as well as the thrust losses due to the contraction of the cross sectional area reaches about 15%. Furthermore, Fig. 13(c) highlighted that 2D CFD computations (red line) underestimated the I_{sp}-efficiency with respect to the analytical model (blue line) of about 10%, despite the larger boundary layer thicknesses. This is due to the different isentropic results which were evaluated at two different location, namely at the micronozzle exit in cases involving the 1D modeling and in the plume for CFD computations. As previ-

ously discussed, these findings are strictly related to the absence of any 3D effect in 2D CFD computations, which were partly considered by the semi-empirical relations (17)-(21) of the one-dimensional model. On the other hand, the 2D CFD and the 1D model provided a quite similar prediction of the discharge coefficient, as shown in Fig. 13(d).

5.3. Assessment of 3D viscous losses into the micronozzle

The analysis of the micronozzle flow was extended by means of 3D computations with maxwellian slip applied to the entire micronozzle (SIM2-3D). In fact, due to growth of the boundary layer along the depth-wise direction the flow blockage took place inside the micronozzle, as highlighted in Fig. 15. Furthermore, the strong expansion ratio at the nozzle exit originated an expansion fan close to the lips of the micronozzle, and the reflected expansion waves formed a set of oblique shock waves into the jet plume. As a result, a small Mach disk formed inside the plume followed by a subsonic recirculation region. In particular, the nozzle blockage produced a strong decrease of the Mach number during the flow expansion process into the divergent section and the rapid growth of the boundary layer thicknesses along the width-wise direction. This phenomenon is depicted in Fig. 16(a), which compares the displacement thicknesses (blue lines) and the momentum thicknesses (red lines) developed along the width-wise and the depth-wise directions. In particular, the growth of the thicknesses along the micronozzle exhibited a peak before the nozzle exit corresponding the maximum thickness of the subsonic pocket showed in Fig. 15(b)-Plane A. Conversely, the 2D boundary layer thicknesses (test case SIM2-2D) linearly grew along the slanted walls of the micronozzle, as shown in Fig. 16(b), highlighting the nonlinear effects of the nozzle blockage.

Instead, along the depth-wise direction the displacement thickness δ^* reached about 20 µm, which corresponds to almost one third of the semi-depth of the micronozzle. The nozzle blockage also caused the viscous heating highlighted in Fig. 17, which compares the temperature field inside the micronozzle between the 2D solution (Fig. 17(a), SIM2-2D) and the 3D one (Fig. 17(b), SIM2-3D).

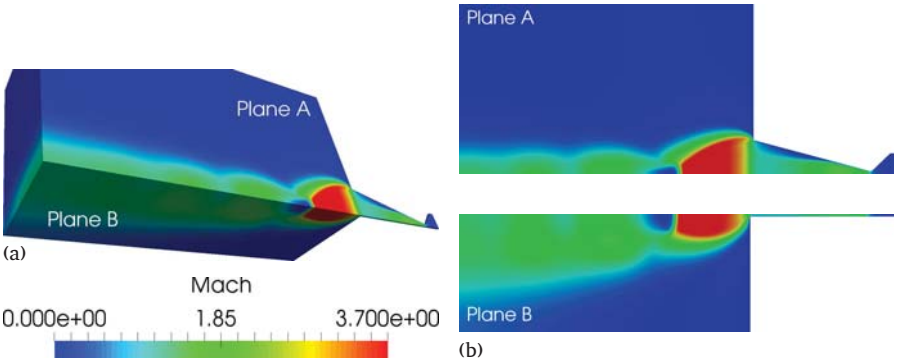

Figure 15: 3D field of the Mach number of the test case SIM2-3D.

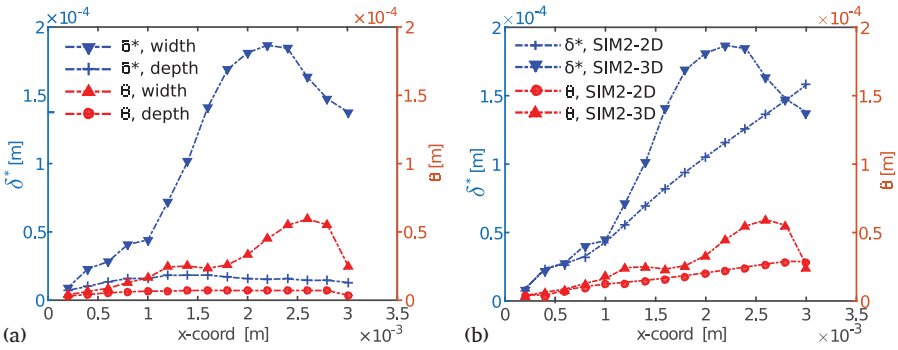

Figure 16: Axial profiles of the boundary layer thicknesses (BLTs) δ^* (blue lines) and θ (red lines) predicted by CFD computations: (a) comparison between the 3D BLTs along the width and depth directions (SIM2-3D); (b) comparison of the width-wise BLTs between the 2D test case (SIM2-2D) and the 3D test case (SIM2-3D)

The viscous heating was responsible of the thermal chocking of the supersonic flow. Consequently, the jet thrust reduced in favor of the pressure at the exit of the micronozzle, so as to produce a relevant reduction of the actual thrust produced by the microthruster. This finding confirmed that the viscous blockage strongly impacts the flow inside the micronozzle yet it cannot be easily retrieved by means of direct measure of the jet thrust of the plume.

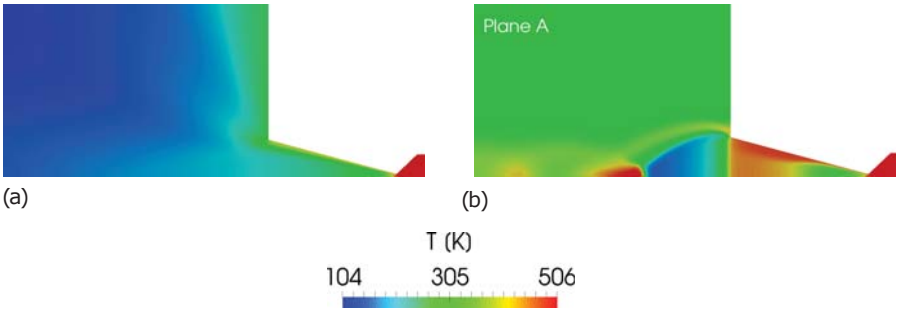

Figure 17: Contours of the temperature field T: (a) 2D solution (SIM2-2D); (b) 3D solution on the symmetry plane A (SIM2-3D). Units are in kelvin, [K].

Tab 8 reports the comparison between the numerical thrust force predicted by the 1D model, 2D and 3D CFD investigations with respect to the experiments [22]. Results highlighted the different modeling of the viscous effects

Table 8: Comparisons between numerical predictions and experimental data [22]. F_{IRT}, equal to 6.6 mN, is the thrust force predicted by the ideal rocket theory at the same inlet conditions.

Test Case	$\mathbf{C_d}$, [-]	$\mathbf{F_{EXP}}$, [mN]	$\mathbf{F_{num}}$, [mN]	$\mathbf{F_{num}/F_{IRT}}$, [−]
#7-1D	0.948	5.20	5.46	0.827
SIM2Dslip	0.958	5.20	6.00	0.909
SIM2-2D	0.934	5.20	5.80	0.879
SIM2-3D	0.917	5.20	4.72	0.715

provided by each numerical approach. In particular, the 3D CFD model (SIM2-3D) provided the lowest estimation of the performance, which pointed out the strong relevance of the 3D viscous effects. The lower thrust for the 3D sim-

ulations can be related to the presence of a thicker subsonic boundary layer (see Fig. 16) and to a consequent lower mass flow and low velocity close to the wall. In fact, the 3D CFD model predicted the maximum loss of mass flow rate, which contributed to the reduction of the thrust force in the measure of about 8%. The last one approached the experiments with an error of 9.2% below, contrary to all other models which overestimated the performance. It is worth to underline that flow boiling instabilities affected the experimental thrust, as highlighted in [22]. At about $p_{0,inlet} = 2.1 \times 10^5$ Pa, they showed a pulsating thrust signal with an average value of about 5.12 mN and standard deviation of approximately ± 0.86 mN. This suggests that the 3D CFD prediction of the thrust can still be considered in accordance with experiments, despite the underestimation with respect to the experimental average value. Tab. 8 also provides the ratio between the numerically predicted thrust force and the one resulting from the IRT at the same inlet conditions, namely F/F_{IRT} with $F_{IRT} = 6.6$ mN. It confirmed that the 2D CFD simulations led to the highest ratios as a consequence of the smallest influence of the viscous effects. Conversely, a larger content of viscous losses was estimated by the improved 1D model to the extent of 17.3%, which increased up to 28.5% in case of 3D computations. Finally, the best matching with experiments was provided by the improved 1D model (#7-1D), which underlines that the use of semi-empirical relations in a simplified analytical modeling could be convenient with respect to complex CFD simulations, particularly for an initial estimation of the overall performance of the microthruster.

6. Conclusions

This work presented a novel quasi-one-dimensional model for the prediction of the performance of the Vaporizing Liquid Microthruster and of its components. In particular, the model coupled the analysis of the non-ideal flow inside the micronozzle with a steady-state solution of the boiling flow into the heating chamber, by means of an iterative procedure aiming at the convergence of the

actual mass flow rate and the heat flux. For the purpose, a set of semi-empirical formulas found among both theoretical and experimental scientific works have been introduced for the estimation of the critical heat flux condition and the local heat transfer coefficient. This allowed for an improved characterization of the two-phase flow inside the inlet plenum and the heating chamber. Furthermore, a non-ideal micronozzle model was built on the Ideal Rocket Theory enhanced by the implementation of analytical and semi-empirical formulas for the estimation of the discharge coefficient and the I_{sp}-efficiency in presence of viscous losses. The investigation focused on the VLM developed by Cen [22], whose findings were used for validation and comparisons. In general, results confirmed that the proposed one-dimensional analytical model is able to provide useful insight of the functioning of a VLM in on-design conditions, which correspond to a single-phase vapor exhaust flow at the nozzle exit. Furthermore, the following findings have been retrieved.

- The empirical correlations [42] of the boiling flow into the microchannels allowed the estimation of the local Nusselt number and improved the prediction of the HTC with respect to the case of uniformly distributed Nusselt number with $Nu = 4.96$. This resulted in a faster evaporation process inside microchannels, which led to lower pressure drops and higher temperatures of the vapor at the micronozzle entrance.

- The 1D model predictions well agreed with experiments in both thrust force and specific impulse, with errors below 7.3%.

- The analytical model provided a better global estimation of the performance losses with respect to 2D CFD computations, despite smaller boundary layer thicknesses. This is certainly related to the 3D real flow effects, which are considered in the 1D empirical formulation while they are neglected into the 2D CFD modeling.

- The 3D model prediction of the thrust force approached the experimental thrust with an error of about 9.2% below, pointing out the strong relevance

of the 3D viscous losses in terms of discharge coefficient and I_{sp}-efficiency. Furthermore, the CFD analysis of the 3D supersonic flow revealed a severe viscous reduction of jet thrust in favor of the pressure thrust at the nozzle exit.

- 3D CFD computations also revealed the establishment of the viscous flow blockage and the resulting viscous heating. The viscous heating led to the thermal chocking of the supersonic flow which certainly contributed to the heavy loss of performance. Along the slanted walls of the expander the boundary layer thicknesses exhibited a rapid growth before to decrease at the subsonic pocket exit.

- The analysis of the jet plume highlighted the formation of the Mach disk followed by the typical diamond-shaped subsonic recirculation region.

References

[1] C. Saaj, V. Lappas, H. Schaub, D. Izzo, Hybrid propulsion system for formation flying using electrostatic forces, Aerospace Science and Technology 14 (5) (2010) 348 – 355. doi:https://doi.org/10.1016/j.ast.2010.02.009.

[2] J. Kindracki, K. Tur, P. Paszkiewicz, L. Mezyk, L. Boruc, P. Wolanski, Experimental research on low-cost cold gas propulsion for a space robot platform, Aerospace Science and Technology 62 (2017) 148 – 157. doi:https://doi.org/10.1016/j.ast.2016.12.001.

[3] R. Ranjan, S. K. Chou, F. Riaz, K. Karthikeyan, Cold gas micro propulsion development for satellite application, Vol. 143, 2017, pp. 754 – 761, leveraging Energy Technologies and Policy Options for Low Carbon Cities. doi:https://doi.org/10.1016/j.egypro.2017.12.758.

[4] A. G. Cofer, W. J. O'Neill, S. D. Heister, E. H. Cardiff, A. A. Alexeenko, Film-evaporation microthruster for cubesats, in: 2016 IEEE 29th Interna-

tional Conference on Micro Electro Mechanical Systems (MEMS), 2016, pp. 1248–1251.

[5] J. Liu, D. Liang, Y. Wang, Y. Yang, W. Shi, J. Zhou, Review on mems-based solid propellant micro-propulsion, Nami Jishu yu Jingmi Gongcheng/Nanotechnology and Precision Engineering 14 (1) (2016) 48–54.

[6] A. Cervone, A. Mancas, B. Zandbergen, Conceptual design of a low-pressure micro-resistojet based on a sublimating solid propellant, Acta Astronautica 108 (2015) 30–39. doi:10.1016/j.actaastro.2010.04.009.

[7] J. Huh, D. Seo, S. Kwon, Fabrication of a liquid monopropellant microthruster with built-in regenerative micro-cooling channels, Sensors and Actuators, A: Physical 263 (2017) 332–340.

[8] T. Moeller, Y.-K. Chang, Mach2 simulations of a micro laser ablation plasma thruster, Aerospace Science and Technology 11 (6) (2007) 481 – 489. doi:https://doi.org/10.1016/j.ast.2007.02.002.

[9] N. A. Gatsonis, Y. Lu, J. J. Blandino, M. A. Demetriou, N. Paschalidis, Micro pulsed plasma thrusters for attitude control of a low earth orbiting cubesat, in: 54th AIAA Aerospace Sciences Meeting, 2016, p. 0692.

[10] T. Henning, K. Huhn, L. Isberner, P. Klar, Miniaturized electrospray thrusters, IEEE Transactions on Plasma Science 46 (2) (2018) 214–218.

[11] M. Silva, D. Guerrieri, A. Cervone, E. Gill, A review of mems micropropulsion technologies for cubesats and pocketqubes, Acta Astronautica 143 (2018) 234–243. doi:10.1016/j.actaastro.2017.11.049.

[12] M. Silva, D. Guerrieri, H. van Zeijl, A. Cervone, E. Gill, Vaporizing liquid microthrusters with integrated heaters and temperature measurement, Sensors and Actuators, A: Physical 265 (2017) 261–274.

[13] K. Lemmer, Propulsion for cubesats, Acta Astronautica 134 (2017) 231 – 243. doi:https://doi.org/10.1016/j.actaastro.2017.01.048.

[14] J. Mueller, W. Tang, A. Wallace, R. Lawton, W. Li, D. Bame, I. Chakraborty, J. Mueller, W. Tang, A. Wallace, et al., Design, analysis and fabrication of a vaporizing liquid micro-thruster, in: 33rd Joint Propulsion Conference and Exhibit, 1997, p. 3054.

[15] J. Mueller, D. Bame, I. Chakraborty, A. Wallace, W. Tang, R. Lawton, Proof-of-concept demonstration of a vaporizing liquid micro-thruster, in: 34th AIAA/ASME/SAE/ASEE Joint Propulsion Conference and Exhibit, 1998, p. 3924.

[16] J. Mueller, I. Chakraborty, D. Bame, W. Tang, Vaporizing liquid microthruster concept: Preliminary results of initial feasibility studies, Micropropulsion for small spacecraft, Reston, VA, American Institute of Aeronautics and Astronautics, Inc.(Progress in Astronautics and Aeronautics. 187 (2000) 215–230.

[17] E. Mukerjee, A. Wallace, K. Yan, D. Howard, R. Smith, S. Collins, Vaporizing liquid microthruster, Sensors and Actuators A: Physical 83 (1) (2000) 231 – 236. doi:https://doi.org/10.1016/S0924-4247(99)00389-1.

[18] D. Maurya, S. Das, S. Lahiri, Silicon mems vaporizing liquid microthruster with internal microheater, Journal of Micromechanics and Microengineering 15 (5) (2005) 966.

[19] P. Kundu, T. Bhattacharyya, S. Das, Design, fabrication and performance evaluation of a vaporizing liquid microthruster, Journal of Micromechanics and Microengineering 22 (2).

[20] X. Ye, F. Tang, H. Ding, Z. Zhou, Study of a vaporizing water microthruster, Sensors and Actuators, A: Physical 89 (1-2) (2001) 159–165.

[21] C.-C. Chen, C.-W. Liu, H.-C. Kan, L.-H. Hu, G.-S. Chang, M.-C. Cheng, B.-T. Dai, Simulation and experiment research on vaporizing liquid microthruster, Sensors and Actuators, A: Physical 157 (1) (2010) 140–149.

[22] J. Cen, J. Xu, Performance evaluation and flow visualization of a mems based vaporizing liquid micro-thruster, Acta Astronautica 67 (3-4) (2010) 468–482. doi:10.1016/j.actaastro.2010.04.009.

[23] K. Karthikeyan, S. Chou, L. Khoong, Y. Tan, C. Lu, W. Yang, Low temperature co-fired ceramic vaporizing liquid microthruster for microspacecraft applications, Applied Energy 97 (2012) 577–583.

[24] K. Cheah, K.-S. Low, Fabrication and performance evaluation of a high temperature co-fired ceramic vaporizing liquid microthruster, Journal of Micromechanics and Microengineering 25 (1).

[25] Y. Gao, Y. F. Ma, J. T. Liu, A review of the vaporizing liquid microthruster technology, in: 2014 ISFMFE - 6th International Symposium on Fluid Machinery and Fluid Engineering, 2014, pp. 1–3.

[26] R. L. Bayt, Viscous effects in supersonic mems-fabricated micronozzles, in: 3rd ASME Microfluid Symposium (Anaheim, CA.), 1998, 1998.

[27] W. Louisos, D. Hitt, Viscous effects on performance of two-dimensional supersonic linear micronozzles, Journal of Spacecraft and Rockets 45 (4) (2008) 706–715. doi:10.2514/1.33434.

[28] W. Louisos, D. Hitt, Performance characteristics of 3d supersonic micronozzles, American Institute of Aeronautics and Astronautics, Reston, Va., 2008.

[29] K. Cheah, J. Chin, Performance improvement on mems micropropulsion system through a novel two-depth micronozzle design, Acta Astronautica 69 (1-2) (2011) 59–70. doi:10.1016/j.actaastro.2011.02.018.

[30] E. Sokolov, M. Chernyshov, Optimization of micronozzle performance at zero ambient pressure, Acta Astronautica doi:10.1016/j.actaastro.2017.12.027.

[31] G. Zhang, L. Wang, X. Zhang, M. Liu, Continuum-based model and its validity for micro-nozzle flows, Jisuan Wuli/Chinese Journal of Computational Physics 24 (5) (2007) 598–604.

[32] M. G. De Giorgi, D. Fontanarosa, A. Ficarella, Modeling viscous effects on boundary layer of rarefied gas flows inside micronozzles in the slip regime condition, Energy Procedia 148 (2018) 838–845.

[33] G. A. Bird, Molecular gas dynamics, NASA STI/Recon Technical Report A 76.

[34] H. Sofloo, R. Ebrahimi, A. Shams, Simulation of rarefied gas flows in mems/nems using a molecular method, Vol. 1, 2009, pp. 1039–1044. doi:10.1115/FEDSM2009-78015.

[35] A. Alexeenko, Numerical study of flow structure and thrust performance for 3-d mems-based nozzles, in: 32 nd AIAA Fluid Dynamics Meeting, St. Louis, MO, 2002.

[36] M. Liu, X. Zhang, G. Zhang, Y. Chen, Study on micronozzle flow and propulsion performance using dsmc and continuum methods, Acta Mechanica Sinica/Lixue Xuebao 22 (5) (2006) 409–416. doi:10.1007/s10409-006-0020-y.

[37] M. Magnini, B. Pulvirenti, J. Thome, Numerical investigation of hydrodynamics and heat transfer of elongated bubbles during flow boiling in a microchannel, International Journal of Heat and Mass Transfer 59 (2013) 451 – 471. doi:https://doi.org/10.1016/j.ijheatmasstransfer.2012.12.010.

[38] Z. Guo, B. Haynes, D. Fletcher, Numerical simulation of annular flow boiling in microchannels, The Journal of Computational Multiphase Flows 8 (1) (2016) 61–82. doi:10.1177/1757482X16634205.

[39] D. Maurya, S. Das, S. Lahiri, An analytical model of a silicon mems vaporizing liquid microthruster and some experimental studies, Sensors and Actuators, A: Physical 122 (1 SPEC. ISS.) (2005) 159–166.

[40] M. Bidabadi, M. Heidari, A. Rahbari, A novel analytical model of a mems vaporizing liquid micro thruster: Multi-phase flow and heat transfer, Vol. 5, 2010, pp. 321–325.

[41] M. de Athayde Costa e Silva, S. Silvestrini, D. Guerrieri, A. Cervone, E. Gill, A comprehensive model for control of vaporizing liquid microthrusters, IEEE Transactions on Control Systems Technology PP (2018) 1–8.

[42] C. Tibiriçá, D. Rocha, J. Sueth, I.L.S., G. Bochio, G. Shimizu, M. Barbosa, S. Ferreira, A complete set of simple and optimized correlations for microchannel flow boiling and two-phase flow applications, Applied Thermal Engineering 126 (2017) 774–795. doi:10.1016/j.applthermaleng.2017.07.161.

[43] N. Kuluva, G. Hosack, Supersonic nozzle discharge coefficients at low reynolds numbers, AIAA Journal 9 (9) (1971) 1876–1879. doi:10.2514/3.6443.

[44] D. L. Whitfield, Integral solution of compressible turbulent boundary layers using improved velocity profiles, Tech. rep., ARNOLD ENGINEERING DEVELOPMENT CENTER ARNOLD AFB TN (1978).

[45] D. Guerrieri, M. Silva, A. Cervone, E. Gill, Selection and characterization of green propellants for micro-resistojets, Journal of Heat Transfer 139 (10). doi:10.1115/1.4036619.

[46] T. L. Bergman, F. P. Incropera, Introduction to heat transfer, John Wiley & Sons, 2011.

[47] I. H. Bell, J. Wronski, S. Quoilin, V. Lemort, Pure and pseudo-pure fluid thermophysical property evaluation and the open-source thermophysical property library coolprop, Industrial & Engineering Chemistry Research 53 (6) (2014) 2498–2508. doi:10.1021/ie4033999.

[48] G. P. Sutton, O. Biblarz, Rocket propulsion elements, John Wiley & Sons, 2016.

[49] Y. Çengel, J. Cimbala, Fluid mechanics fundamentals and applications, International Edition, McGraw Hill Publication 185201.

[50] A. Bejan, A. D. Kraus, Heat transfer handbook, Vol. 1, John Wiley & Sons, 2003.

[51] C. Greenshields, H. Weller, L. Gasparini, J. Reese, Implementation of semi-discrete, non-staggered central schemes in a colocated, polyhedral, finite volume framework, for high-speed viscous flows, International Journal for Numerical Methods in Fluids 63 (1) (2010) 1–21. doi:10.1002/fld.2069.

[52] A. Kurganov, E. Tadmor, New high-resolution central schemes for nonlinear conservation laws and convection–diffusion equations, Journal of Computational Physics 160 (1) (2000) 241 – 282. doi:https://doi.org/10.1006/jcph.2000.6459.

[53] B. van Leer, Towards the ultimate conservative difference scheme. v. a second-order sequel to godunov's method, Journal of Computational Physics 32 (1) (1979) 101 – 136. doi:https://doi.org/10.1016/0021-9991(79)90145-1.

[54] D.-Y. Peng, D. B. Robinson, A new two-constant equation of state, Industrial & Engineering Chemistry Fundamentals 15 (1) (1976) 59–64.

[55] NASA, Examining spatial (grid) convergence. (2006).
URL https://www.grc.nasa.gov/www/wind/valid/tutorial/spatconv.html